Modelling of a Bio-inspired Bistable Energy Harvester for Potential Application in Fish Telemetry Tags

Mrunal Bhalerao[a], Muhammad Hajj[b], Lei Zuo*[c]

[a]Dept. of Mechanical Engineering, Virginia Tech, Blacksburg, VA
[b]Dept. of Civil, Environmental and Ocean Engineering, Stevens Institute of Technology, Hoboken, NJ
[c]Dept. of Naval Architecture and Marine Engineering, University of Michigan, Ann Arbor, MI

ABSTRACT

Monitoring of aquatic life is important for assessing long-term impacts on activities associated with fish stock and migration. One promising approach for long-term monitoring involves the development of self-powered telemetry devices capable of powering themselves by harnessing energy from the fish body undulations using implanted devices or from fluid motions generated by fish swimming using external devices. One of the latter devices is a broadband low frequency nonlinear bistable energy harvester. This cost-effective harvester has been inspired from the doubly curved leaf blades of a Venus-fly trap. This work examines the static behavior of such a bio-inspired bistable energy harvester by analyzing its force-displacement characteristics. The objective is to identify crucial design parameters to optimize the harvester's performance for potential application in self-powered fish telemetry tags. The unique characteristics of hysteresis loop and snap-through discontinuity of the harvester are investigated using finite element analysis. The finite element model is found to qualitatively replicate experimental observations. Additionally, geometrical and assembly parameters that affect the force-displacement behavior of the harvester are identified. A sensitivity analysis is performed to determine the effect of the aspect ratio, buckling displacement and thickness of the proposed harvester on the static force-displacement curve.

Keywords: Bio-inspired Bistable Structure (BBS), Static Simulation, Snap-through, Hysteresis loop.

1. INTRODUCTION

The widespread adoption of the concept of the 'Blue Economy' in recent years has underscored the importance of "the sustainable utilization of ocean resources to foster economic development, enhance livelihoods, and generate employment opportunities, all while safeguarding the health of marine ecosystems" [1]. This has prompted the need to advance the design of telemetry tags capable of long-term monitoring of aquatic systems to assess ecological impacts of said water-based economic activities.

Over the past decade, there have been numerous initiatives focused on acoustic aquatic telemetry [2-12]. Among these efforts, there's a growing focus on developing self-powered telemetry tags, aimed at facilitating long-term monitoring that would not depend on depletable batteries. Such an advancement would make technology viable even for smaller fish. For instance, Alqaleiby et al. [7] determined that because of the low energy harvested by a piezoelectric element, attaching a piezoelectric energy harvester does not impact the swimming activities of a fish. Cha et al. [8] explored the feasibility of harvesting energy from the motion of a robotic fishtail modelled to replicate the swimming pattern of a thresher shark utilizing bimorph piezoelectric beams, while Li et al. [9] demonstrated, through experiments on robotic and live chinook salmon fish, the viability of sub-dermally embedded piezoelectric harvesters. Qian et al. [10] suggested externally attaching the harvester to the concerned aquatic species and deriving energy from base excitations due to fish maneuvering, flow-induced vibrations from the fish swimming in water and other random disturbances in the aquatic environment.

Due to the multitude of sources of excitation, an externally attached harvester is expected to be exposed to a relatively wide range of excitation frequencies whose energy must be effectively harvested. The effectiveness of bistable systems, a subset of non-linear systems, in harvesting energy across a broad frequency range from the ambient environment has been well-documented [13], with various methods employed to enable them [13-14]. The distinctive sensitivity of bistable systems to a broad spectrum of excitation frequencies has led to many investigations into the dynamic behavior of the bistable system [15-22]. Moreover, there have been few trials to numerically simulate the static behavior of such systems [16]. For instance, Abbasi et al. [18] and Amor et al [20] developed analytical models for simple buckling-based bistable systems.

Active and Passive Smart Structures and Integrated Systems XVIII, edited by Serife Tol, Guoliang Huang,
Xiaopeng Li, Mostafa A. Nouh, Shima Shahab, Jinkyu Yang, Proc. of SPIE Vol. 12946,
129460Y · © 2024 SPIE · 0277-786X · doi: 10.1117/12.3011010

Qian et al. [10,15] introduced a novel, bi-directionally curved bistable energy harvester inspired by the leaf blades of the Venus flytrap, showcasing its proof of concept. Unlike previous bistable systems [13-14], this innovative design is self-contained and does not require an external mechanism to induce bi-stability. Expanding upon the self-contained bistable system introduced by Qian et al. [10,15], we propose a modified version of the harvester replicating the features of a hairclip to enhance repeatability and ensure cost-effectiveness. While Qian et al. [10] provided a proof of concept for the bio-inspired, bistable energy harvester (BBEH) consisting of the piezoelectric transducer and the bio-inspired, bistable structure (BBS), this paper delves deeper into the static behavior of the BBS to understand its unique snap-through phenomenon and hysteresis loop. The authors believe that this extensive study and assessment of the static behavior of the system, along with the identification of the design parameters influencing its stiffness curve will advance in the tag's design for fishes of varied swimming patterns and speeds.

This paper is structured into six sections. Section 2 details the experimental setup and methodology for recording the stiffness curve of the proposed BBS. Section 3 explains the finite element methodology used for generating the stiffness curve, including a discussion of the boundary conditions and visual representations of buckling mode and post-buckling behavior. In Section 4, parameters affecting the features of the stiffness curve are identified and a sensitivity analysis is performed to study the impacts of the parameters on the stiffness curve. Section 5 compares the results obtained from experimentation and finite element analysis (FEA), exploring reasons for any discrepancies. Finally, Section 6 summarizes the main findings of the paper.

2. EXPERIMENTATION

The concept used in the fabrication of the BBS is schematically presented in Figure 1. An open area was cut from a 0.3mm thick sheet of zinc galvanized low carbon steel and the bi-stability in the BBS was introduced by forcing an in-plane displacement at the split end of the harvester as shown in Figure 1. The buckled BBS exhibited bi-directional curvature as shown in Figure 2. After the in-plane displacement was induced, the two split ends of the BBS were fixed to a rigid mounting structure as shown in Figure 2.

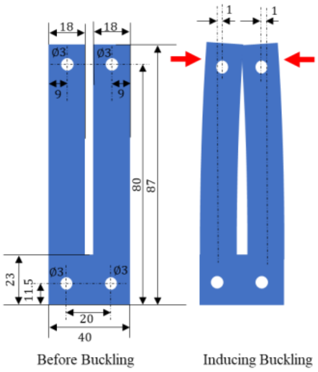

Figure 1: Dimensions of the blank in mm (Thickness is 0.3mm) and direction of in-plane force to induce buckling.

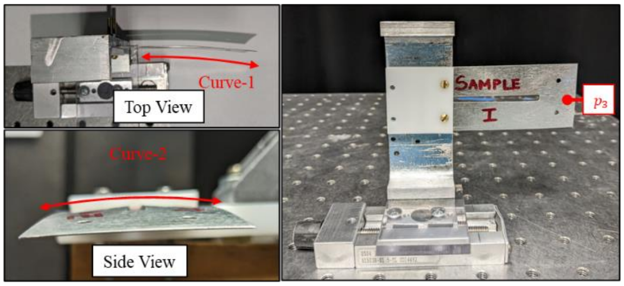

Figure 2: Proposed bio-inspired bistable system exhibiting bidirectional curvature.

As shown in Figure 3, the load cell, which slides on the guiding rails, was controlled by the rotation of the ball screw. The probe from the load cell measures the reaction force while also providing static displacement to the BBS at point p_3 which is measured by the Vernier caliper connected to the load cell (as shown in Figure 3).

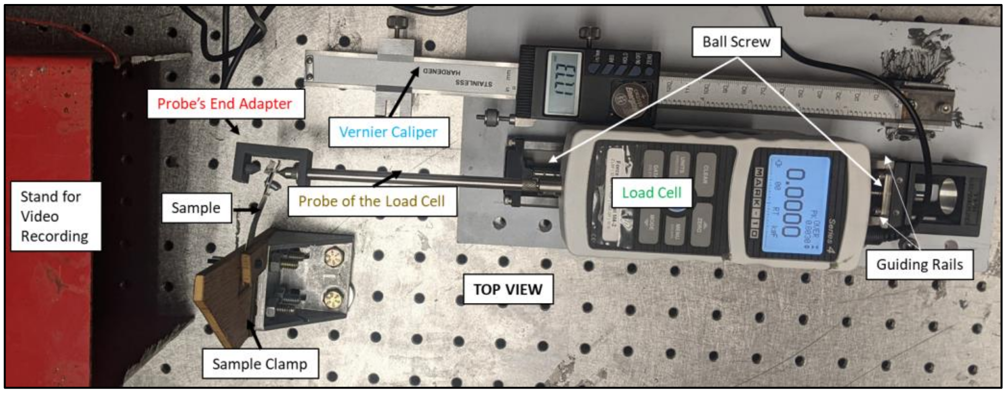

Figure 3: Experimental set-up for measuring the stiffness of the proposed bio-inspired bistable system.

To develop the stiffness curve, gradual and small increments in the range of 0.1-0.2 mm were given to point p_3 by means of the probe and the reaction force is recorded at every increment. The gradual and small increments helped maintain the system in quasistatic equilibrium and ensured repeatable and reliable results. The force was considered positive if the force detected by the load cell was tensile in nature, (i.e. tends to move the probe leftwards in Figure 3), while the force was considered negative if the force detected by the probe was compressive in nature, (i.e. tends to move the probe rightwards in Figure 3). Similarly, the displacement was considered zero in the unstable equilibrium position, while all displacements on the load cell side were considered negative (Figure 3) and all the displacements in the video recorder side were considered positive (Figure 3). Figure 4 below gives the experimental stiffness curve of the BBS.

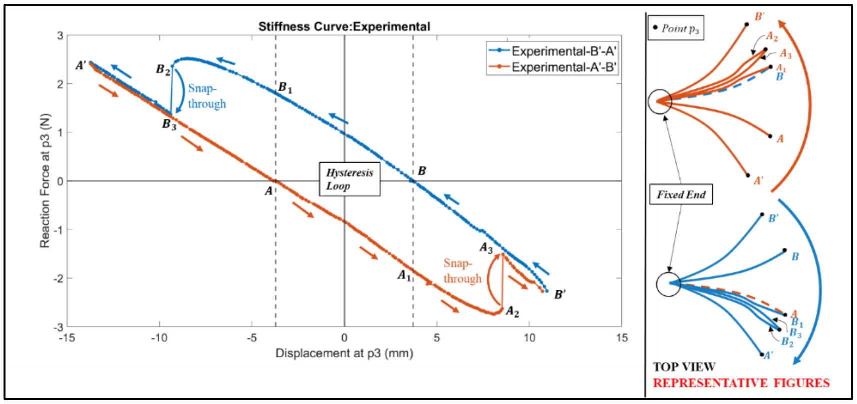

Figure 4: Experimental stiffness curve exhibiting Snap-Through, Hysteresis Loop and Representative Figures of the Top View of the BBS as Point p_3 is Swept from $A' - B'$ and $B' - A'$.

The hysteresis loop ($A_3 - B - B_1 - B_2 - B_3 - A - A_1 - A_2$) and the snap-through are two unique phenomena of the stiffness curve found experimentally. The two stable configurations of the BBS occur at A and B when the reaction force becomes zero. The distance between the two stable equilibrium positions observed is 7.43mm. For the sake of this paper, the term 'configuration' refers to the overall shape of the BBS as seen in the top view for a particular displacement of point p_3.

When point p_3 on the BBS (Figure 2) is swept from A' to B', snap-through occurs at points $A_2 - A_3$. At A_2 and A_3 , the displacement of point p_3 on the sample is almost the same but the configuration changes as shown on the right-hand side of Figure 4 and Figures 5 (c) and 5 (d). Similarly, when point p_3 on the sample is swept from B' to A' the snap through occurs at points $B_2 - B_3$. The hysteresis loop occurs because between the two snap-through positions $A_2 - A_3$ and $B_2 - B_3$, in this region, at every position of point p_3, two different configurations of the BBS are feasible, each exerts a different reaction force. However, the configuration depends on the direction of sweep. For instance, in Figure 5(a) the configuration at B is shown and in Figure 5(b) the configuration at A_1 is shown. The position of the probe is the same for both configurations, however the shape of the BBS is different hence the reaction force is different.

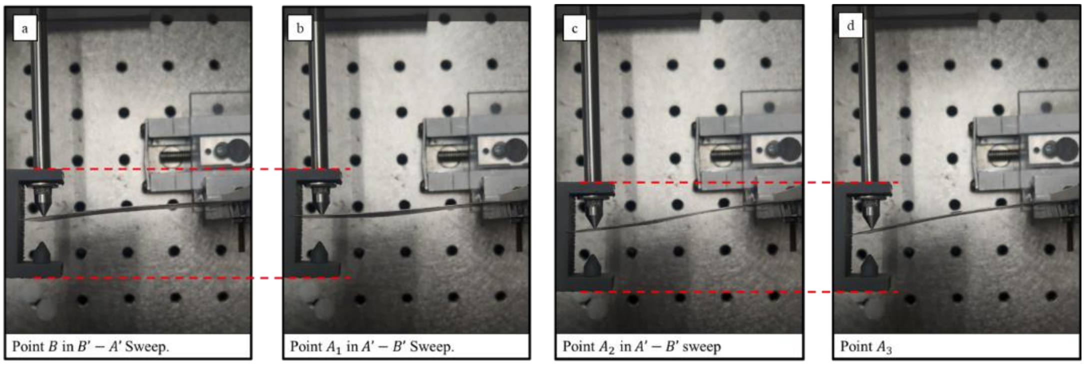

Point B in $B' - A'$ Sweep.

Point A_1 in $A' - B'$ Sweep.

Point A_2 in $A' - B'$ sweep

Point A_3

Figure 5 (a) BBS configuration at B in sweep B'-A'. (b) BBS configuration at A1 in sweep A'-B'. (c) BBS configuration at A2 in sweep A'-B'. (d) BBS configuration at A3.

3. FINITE ELEMENT ANALYSIS

A beam that is bent in the plane of greatest flexural rigidity may buckle laterally at a certain critical value of the load [23]. This type of buckling has been termed as lateral buckling or lateral torsional buckling in literature [22,23]. The FEA-based static analysis of the BBS was performed in ANSYS utilizing the 'Eigenvalue Buckling' and 'Static Structural' toolboxes. The dimensions of the blank are the same as presented in Figure 1. The material properties for zinc galvanized low carbon steel are presented in Table 1. The meshing for the BBS was performed using TET10 with a mesh size of 1mm. The mesh sizing was determined using mesh convergence and efficiency analysis. First, the buckling modes were identified under the condition of in-plane deflection of points p_{2a} and p_{2b} of the blank as shown in Figure 6. It is identified that the buckling mode shown in Video 1 is the relevant mode and has been used to generate the buckled state of the sample. Since buckling is an eigenvalue problem, in order to obtain a unique solution of lateral displacement an initial geometric imperfection was introduced before the post buckling analysis. The amount of the imperfection was calibrated based on the lateral displacement of point p_3 in the stable equilibrium position observed experimentally.

Post-buckling analysis was performed to generate the stiffness curve. In the post-buckling analysis lateral deflection was induced at point p_3 and the reaction force in the lateral direction as exerted at the point of application of the displacement was measured. Figure 6 shows the various points at which the boundary conditions were applied to the sample.

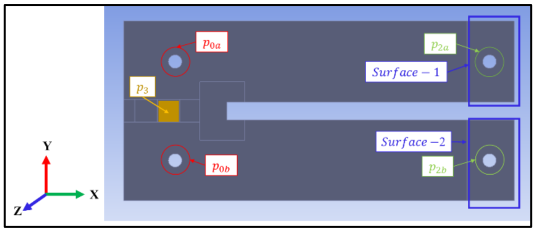

Figure 6: Points of application of boundary conditions for the post-buckling analysis.

The boundary conditions were set as follows:

1. Points p_{0a} and p_{0b} have all translational and rotational degrees of freedom restricted.
2. Points p_{2a} and p_{2b} are given displacements of 1mm towards the centerline of the BBS.
3. The displacements of $surfaces\ 1\ and\ 2$ were constrained in all three translational degrees of freedom (X, Y, Z) and the rotational degrees of freedom about the X and Y axis were restricted (R_x, R_y) allowing motion about the Z axis. This mimics the experimental assembly condition where the highlighted surfaces are used for clamping and fixing the BBS to the BBS mount.
4. The displacement restriction at p_{0a} and p_{0b} was removed so that the BBS goes from its unstable equilibrium position to its stable equilibrium state.

5. Then lateral deflection (perpendicular to the plane of the paper) was applied at point p_3 and the reaction in the lateral direction was measured at p_3.

Videos 2 and 3 demonstrate the post buckling behavior of the system.

Table 1: Material Properties of Zinc Galvanized Low Carbon Steel [24].

Material Property	**Value**	**Unit**
Young's Modulus	2.075×10^{11}	$\frac{N}{m^2}$
Poisson's Ratio	0.29	–
Bulk Modulus	1.65×10^{11}	$\frac{N}{m^2}$
Shear Modulus	8.04×10^{10}	$\frac{N}{m^2}$

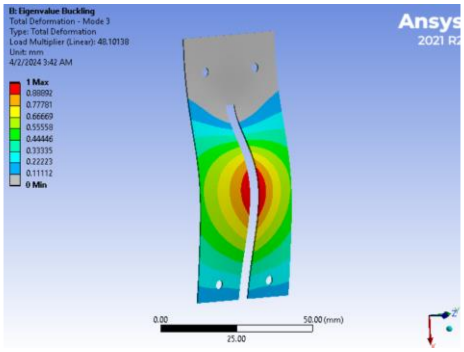

Video 1: Relevant mode of buckling (http://dx.doi.org/10.1117/12.3011010.1)

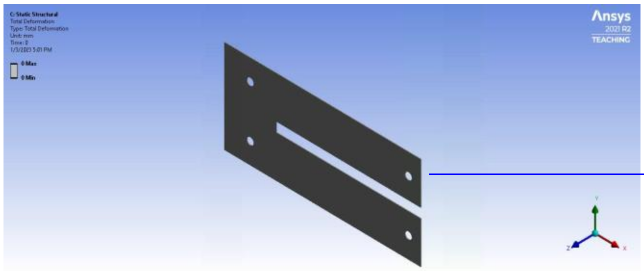

Video 2: Isometric view of buckling and post buckling behavior. (http://dx.doi.org/10.1117/12.3011010.2)

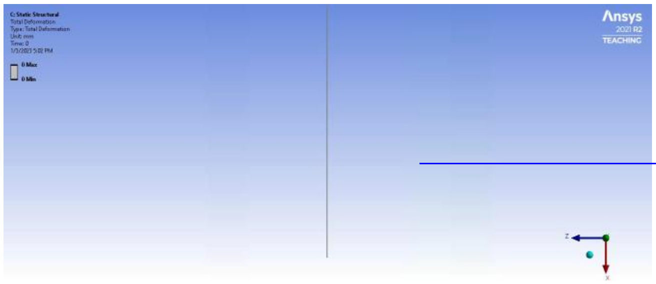

Video 3: Top View of Buckling and Post Buckling Behavior. (http://dx.doi.org/10.1117/12.3011010.3)

The generated stiffness curve is presented in Figure 7. The spikes that are observed at the snap-through stages $A_2 - A_3$ and $B_2 - B_3$ are due to the numerical instability present at that point. Points A and B denote the stable equilibrium points where the reaction force is zero. The FEA based stiffness curve was tuned via the initial imperfection parameter to ensure that the stable equilibrium positions obtained via FEA match closely to the ones obtained experimentally. After optimal tuning, the distance between the stable states in FEA is 10.759 mm compared to the 7.43mm observed experimentally. Hence, although the stiffness curve obtained through FEA qualitatively has similar features to the one obtained experimentally, there are certain quantitative discrepancies that are discussed in detail in Section 5.

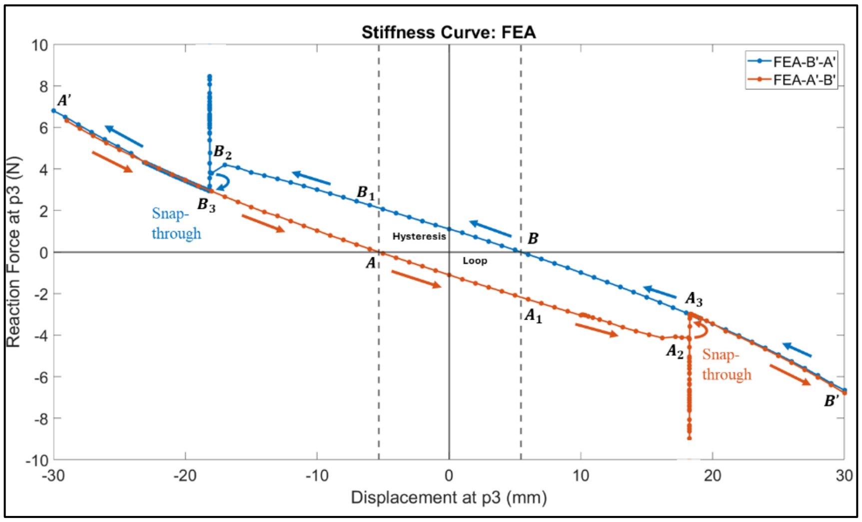

Figure 7: FEA based stiffness curve exhibiting snap-through and hysteresis loop.

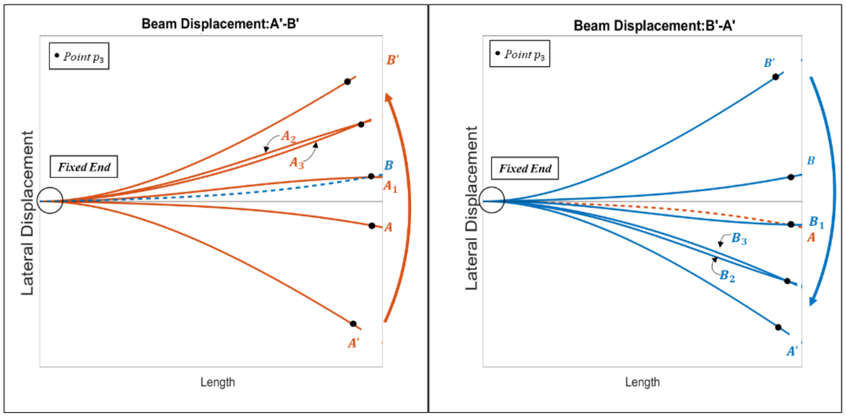

Figure 8: Figures of the top view of the BBS as point p_3 is swept from $A' - B'$ and $B' - A'$.

Figure 8 shows that the configurations of the BBS for different displacements of point p_3 are identical to experimental observations shown in Figures 4 and 5. As point p_3 on the BBS is swept from A' to B', it attains stable equilibrium at A and proceeds further to A_1. At A_1 point p_3 has the same position as in the stable equilibrium state B but the configurations of the BBS are different; hence, the reaction forces are different. As such, in the sweep from A' to B' the stable equilibrium state of B is never reached. Similarly in the sweep from B' to A' the stable equilibrium state of A is never reached.

4. SENSITIVITY ANALYSIS

The stiffness curve of the proposed BBS is sensitive to the geometric as well as the assembly parameters of the BBS. The geometric parameters that strongly affect the stiffness include the aspect ratio ($\frac{L_{active}}{w}$) and the thickness (t) of the BBS, while the assembly parameter affecting the stiffness curve includes the buckling displacement (d). In this section, the sensitivity of the stiffness curve to the aspect ratio, thickness and buckling displacement is determined using FEA. Figure 9 and Table 2 show the aspect ratio, buckling displacement and thickness with reference to the proposed BBS.

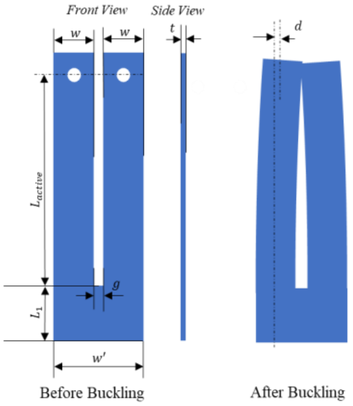

Figure 9: Geometric and assembly parameters for sensitivity analysis

Table 2: Details of the geometrical and assembly parameters

	Dimension	Value
Geometrical Parameters	w	Sub-beam Width
	L_{active}	Active Length
	t	Thickness
Assembly Parameters	d	Buckling Distance

The stiffness curve of the proposed BBS is complex; hence five major features of the stiffness curves are identified which adequately describe the characteristic hysteresis loop and the snap-through phenomenon and also enable comparison between two stiffness curves. These features are highlighted in Figure 10 and can be described as follows:

1. Distance between stable equilibrium states (mm): As point p_3 is swept from $A' - B'$ or $B' - A'$ the BBS achieves stable equilibrium at the position of p_3 where the reaction force at p_3 is zero. The proposed BBS has two stable states. This feature is the absolute distance between the position of point p_3 when the BBS is in each of the stable equilibrium configurations.
2. Distance between the snap-through states (mm): This is the gap between the positions at which the snap-through occurs. The snap-through occurs at $A_2 - A_3$ when point p_3 on the BBS is being swept from $A' - B'$ and it occurs at $B_2 - B_3$ when p_3 is being swept from $B' - A'$.
3. Residual force at unstable equilibrium (N): The unstable equilibrium is observed at the midpoint between the two stable equilibrium positions. The residual force is the sum of the absolute value of the reaction force measured at the unstable equilibrium position when point p_3 on the BBS is swept from $A' - B'$ and $B' - A'$. This feature is a measure of the dimensions of the hysteresis loop.
4. Slope of the trendlines of the hysteresis curve: The hysteresis loop is bound horizontally by the snap-through states while vertically it is bound by $A_3 - B - B_1 - B_2$ and $B_3 - A - A_1 - A_2$. This feature is the average slope of the linear curve fit on the vertical bounds and gives the average stiffness of the hysteresis loop.
5. Approximate area of the hysteresis loop (N.mm): The approximate area of the hysteresis loop is given by the product of the residual force at the unstable equilibrium states (mm) and the distance between the snap through states (mm). The area enclosed in the hysteresis loop is indicative of the non-linearity of the BBS.

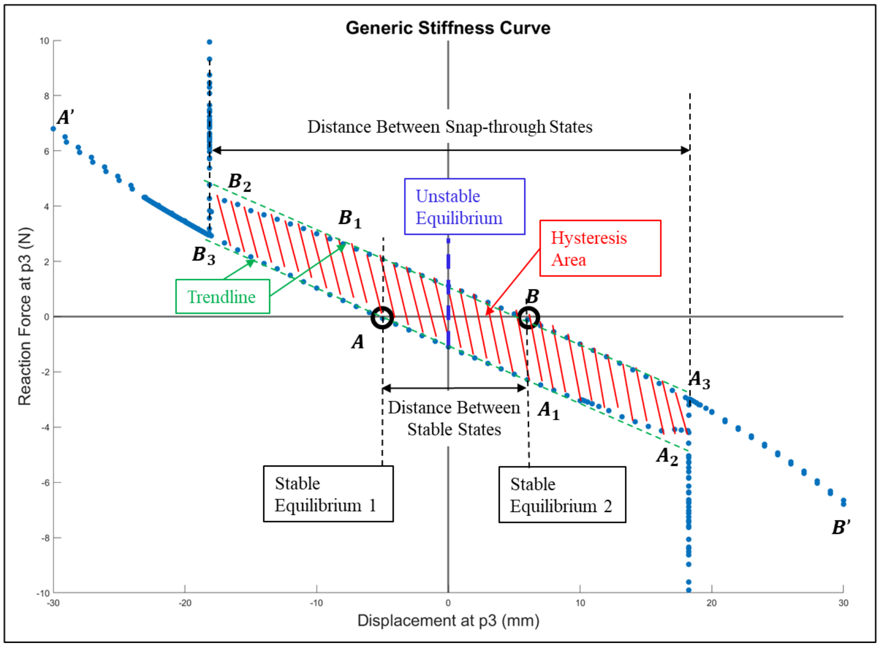

Figure 10: Features of a generic stiffness curve.

4.1 Aspect Ratio:

The aspect ratio for the purpose of this work is defined as the ratio between the active length of the sub-beams to the width of the sub-beam. The active length of the sub-beam is the distance between the point of application of the buckling force and the base of the sub-beam as shown in Figure 9.

Table 3 tabulates the major features of the stiffness curves pertaining to each aspect ratio and Figure 11 shows the stiffness curves as the aspect ratio changes while the other parameters remain constant based on the dimensions shown in Figure 1. The variation in the aspect ratio has been achieved by varying the active length of the BBS.

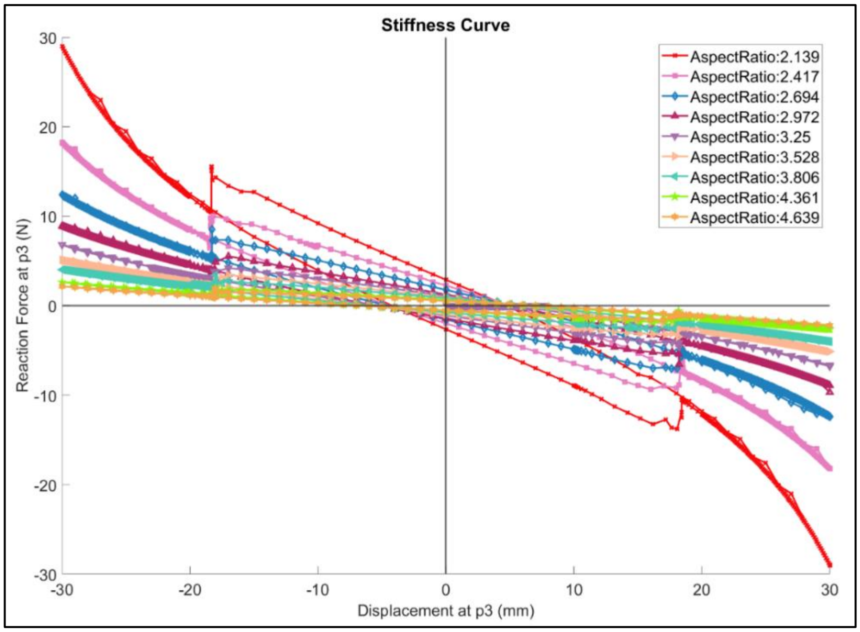

Figure 11: Stiffness curves for different aspect ratios.

Table 3: Major parameters in the stiffness curve for each aspect ratio

Sr. No	**Aspect Ratio**	**Distance Between Stable Equilibrium States (mm)**	**Distance Between Snap Through States (mm)**	**Residual Force at Unstable Equilibrium (N)**	**Avg Slope of the Trendlines of the Hysteresis Curve (N/mm)**	**Approx Hysteresis Area (N.mm)**
1	2.14	8.89	36.75	5.53	-0.66	203.25
2	2.42	9.31	36.91	4.24	-0.47	156.31
3	2.69	9.70	36.70	2.98	-0.35	109.35
4	2.97	10.20	36.47	2.68	-0.26	97.69
5	3.25	10.76	36.38	2.21	-0.20	80.40
6	3.53	11.62	36.37	1.92	-0.16	69.65
7	3.81	12.13	36.28	1.57	-0.13	57.12
8	4.36	13.13	36.18	1.19	-0.09	43.07
9	4.64	13.63	36.10	1.05	-0.08	37.87

Figure 12 shows the variation of the features of the stiffness curve with the aspect ratio. An increase in the active length of the BBS leads to an increase in the distance between the stable equilibrium states (y_1), which varies linearly with the aspect ratio (x_1) as $y_1 = 1.97x_1 + 4.52$ with a coefficient of determination (R^2) of 0.994 as presented in Figure 12 (a). As the aspect ratio increases the BBS becomes slenderer thus decreasing its overall stiffness, hence the slope of the hysteresis loop increases, and the stiffness curve tends to become flatter as expected. Figure 12 (b) shows the slope of the hysteresis curve (y_2) vs the aspect ratio (x_1). A cubic polynomial is fitted to the data in Figure 12 (b) which gives $y_2 = 0.056x_1^3 - 0.69x_1^2 + 2.9x_1 - 4.24$ with a coefficient of determination (R^2) of 0.9988. The distance between the snap through states (y_3) reduces marginally with aspect ratio (x_1) as presented in Figure 12 (c) but there is no strong correlation between the two.

Increasing the aspect ratio of the BBS increases its slenderness and diminishes its non-linear behavior. This is evident in Figure 11, where the size of the hysteresis loop reduces as the aspect ratio increases. The residual force at the unstable equilibrium (y_4) and the approximate area enclosed in the hysteresis loop (y_5) both vary quadratically with the aspect ratio (x_1) as $y_4 = 0.83x_1^2 - 7.23x_1 + 16.93$ and $y_5 = 30.83x_1^2 - 286.77x_1 + 627.02$, with a coefficient of determination (R^2) of 0.9767 and 0.9774 respectively.

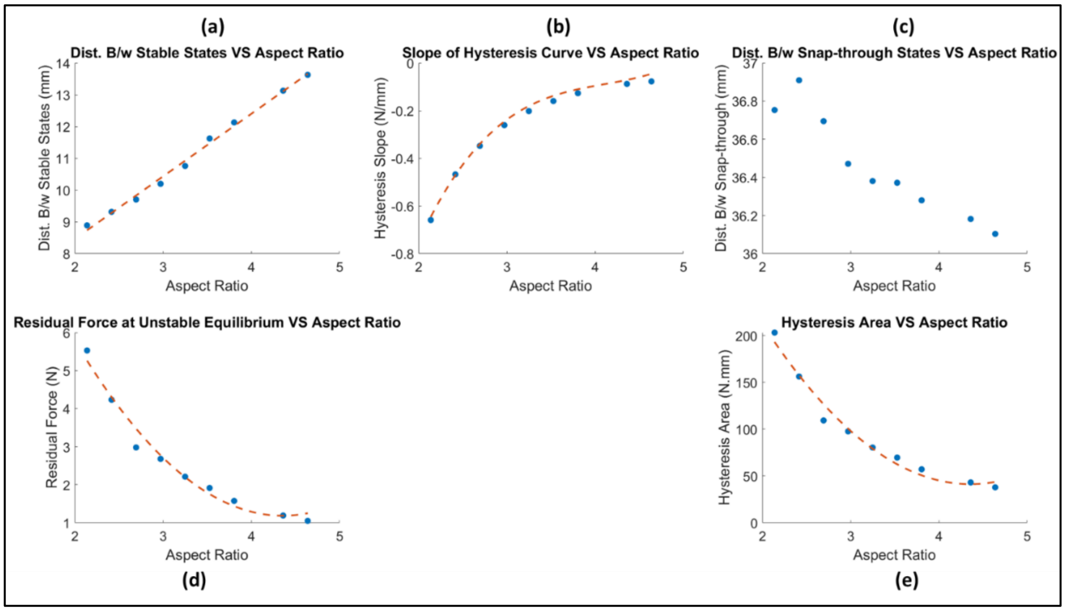

Figure 12: Variation of the parameters of the stiffness curve with the aspect ratio.

4.2 Thickness:

The thickness (t), as shown in Figure 9 is the thickness of the sheet metal used to assemble the BBS. Table 4 tabulates the major features of the stiffness curves pertaining to each thickness. For the overall dimensions and material properties of the BBS being analyzed in this paper, thicknesses between 0.3 mm and 0.5mm are only feasible. Thicknesses below 0.3 mm are very flimsy and undergo plastic deformation during their assembly phase when the buckling is being induced. Thicknesses above 0.5mm require very large forces to induce snap-through (beyond 20N), which is not feasible for the application being considered. Figure 13 shows the stiffness curves as the thickness changes while all other parameters are kept constant and assume the dimensions presented in Figure 1.

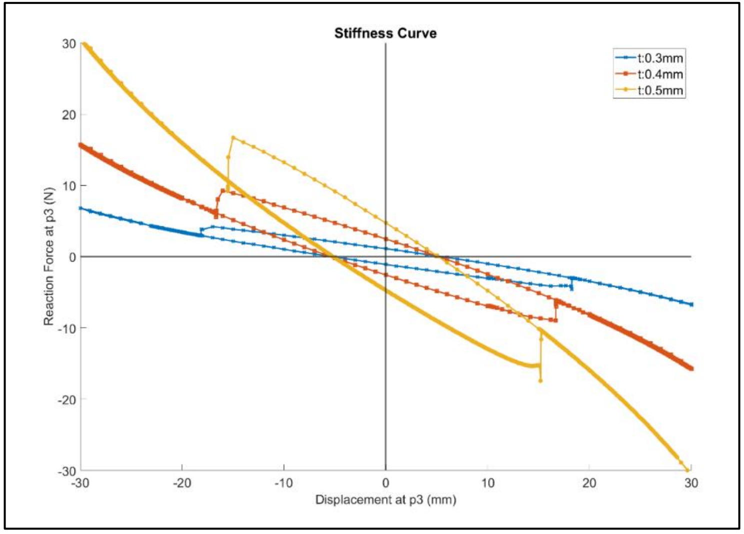

Figure 13: Stiffness curves for different thickness values.

Table 4: Major parameters in the stiffness curve for each thickness value

Sr. No	Thickness (mm)	Distance Between Stable Equilibrium States (mm)	Distance Between Snap Through States (mm)	Residual Force at Unstable Equilibrium (N)	Avg Slope of the Trendlines of the Hysteresis Curve (N/mm)	Approx Hysteresis Area (N.mm)
1	0.3	10.76	36.38	2.21	-0.20	80.40
2	0.4	10.55	33.31	5.05	-0.46	168.07
3	0.5	10.31	30.66	9.44	-0.89	289.54

Figure 14 shows the variation of the features of the stiffness curve with the thickness. Since only three thicknesses were considered, the relationships developed between the features of the stiffness curve and thickness are determined to be strictly linear because fitting a curve with a higher degree polynomial will lead to over-fitting. The distance between the stable states (y_1) decreases marginally with the increase in thickness (x_2) as $y_1 = -2.24x_2 + 11.44$ with a coefficient of determination (R^2) of 0.9979. Overall, it is observed that as the thickness increases, the average stiffness of the BBS increases hence the average slope of the trendlines of the hysteresis loop (y_2) decreases linearly with thickness (x_2) as $y_2 = -3.43x_2 + 0.85$ with a coefficient of determination (R^2) of 0.9818. The increase in thickness (x_2) causes the residual force at the unstable equilibrium position (y_4) to increase more rapidly than it causes the reduction in the distance between snap-through states (y_3). Consequently, this results in a net increase in the area enclosed within the hysteresis loop (y_5) as thickness (x_2) increases which implies that an increase in thickness also tends to make the BBS more non-linear. Consequently, the distance between the snap-through states (y_3), residual force at the unstable equilibrium position (y_4) and the area enclosed in the hysteresis loop (y_5) vary linearly with thickness (x_2) as $y_3 = -28.56x_2 + 44.89$, $y_4 = 36.16x_2 - 8.9$ and $y_5 = 1045.7x_2 - 238.95$ respectively with a coefficient of determination (R^2) of 0.9959, 0.9847 and 0.9914 respectively.

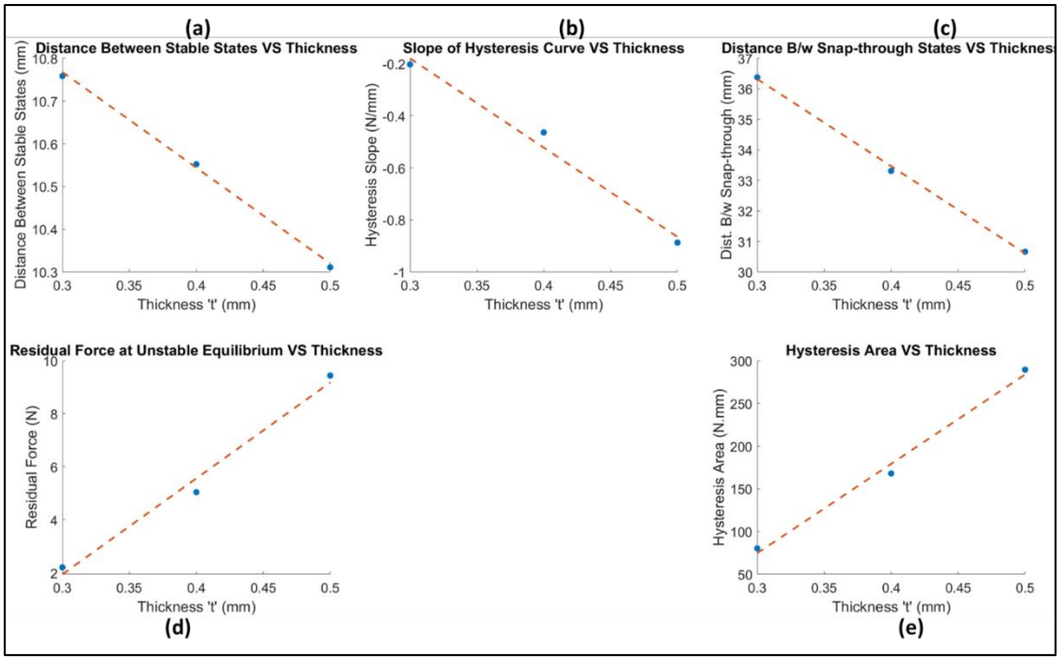

Figure 14: Variation of the parameters of the stiffness curve with the thickness.

4.3 Buckling Displacement:

The buckling displacement (d) of the BBS is an assembly parameter. As shown in Figure 9, 'd' is the in-plane displacement given to the two split ends of the BBS to induce buckling. For the proposed BBS, the buckling displacement can vary from 0 mm to 2mm only. A negative buckling displacement would imply applying an in-plane displacement to the split ends of the structure, which tends to move the split ends away from the centerline of the structure. This leads to a different type of bistable structure which is out of scope of this effort. The split ends of the structure are 4mm apart as seen from Figure 1, thus a buckling displacement of greater than 2mm will cause the split ends to overlap. Although this arrangement is feasible, such an overlap introduces unpredictable friction between the two sub-beams of the BBS which ultimately leads to non-repeatable stiffness curves and a higher rate of wear of the BBS which is undesirable. Table 5 tabulates the major features of the stiffness curves pertaining to each buckling displacement value. Figure 15 shows the stiffness curves as the buckling displacement changes while all other parameters are kept constant.

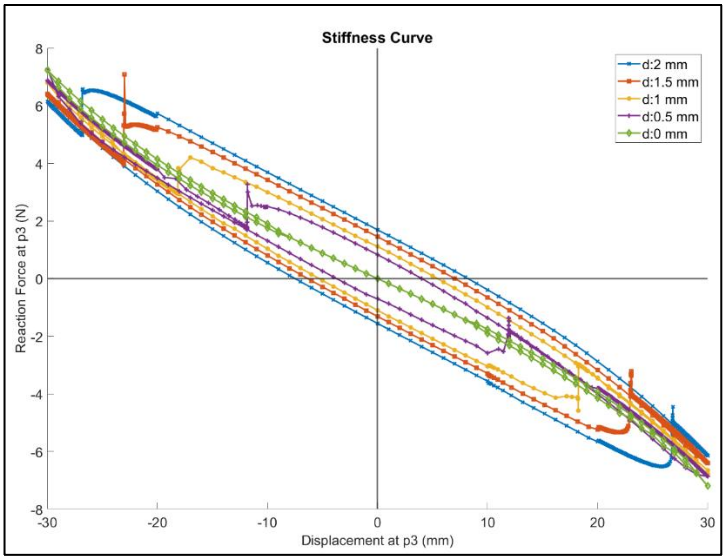

Figure 15: Stiffness curves with varying buckling displacement.

Table 5: Major parameters in the stiffness curve for each buckling displacement value

Sr. No	Buckling Displacement (mm)	Distance Between Stable Equilibrium States (mm)	Distance Between Snap Through States (mm)	Residual Force at Unstable Equilibrium (N)	Avg Slope of the Trendlines of the Hysteresis Curve (N/mm)	Approx Hysteresis Area (N.mm)
1	0	0.00	0.00	0.00	-0.21	0.00
2	0.5	7.74	23.75	1.53	-0.19	36.39
3	1	10.76	36.38	2.21	-0.20	80.40
4	1.5	13.37	46.09	2.77	-0.20	127.42
5	2	15.70	53.63	3.25	-0.21	174.23

Figure 16 shows the variation in the features of a stiffness curve with buckling displacement. The distance between the stable equilibrium states (y_1) increases quadratically with the buckling displacement (x_3) as $y_1 = -3.2x_3^2 + 13.82x_3 + 0.51$ with a coefficient of determination (R^2) of 0.9849. The overall stiffness of the of the BBS, which is estimated by the measure of the average slope of the trendlines of the hysteresis curve (y_2) does not depend very strongly on the buckling displacement (x_3) and has an average value of -0.2016 with a standard deviation of 0.0078. The buckling displacement of the BBS directly influences its non-linear behavior. As the buckling displacement increases, several key indicators of non-linearity like the distance between snap-through states (y_3), residual force at unstable equilibrium (y_4), area enclosed within the hysteresis loop (y_5) also increase. The variations of these key indicators of non-linearity with the buckling displacement are given by $y_3 = -10.74x_3^2 + 47.86x_3$, $y_4 = -0.63x_3^2 + 2.81x_3 + 0.09$ and $y_5 = 87.9x_3 - 4.21$ with a coefficient of determination (R^2) of 0.9949, 0.9894 and 0.9976 respectively.

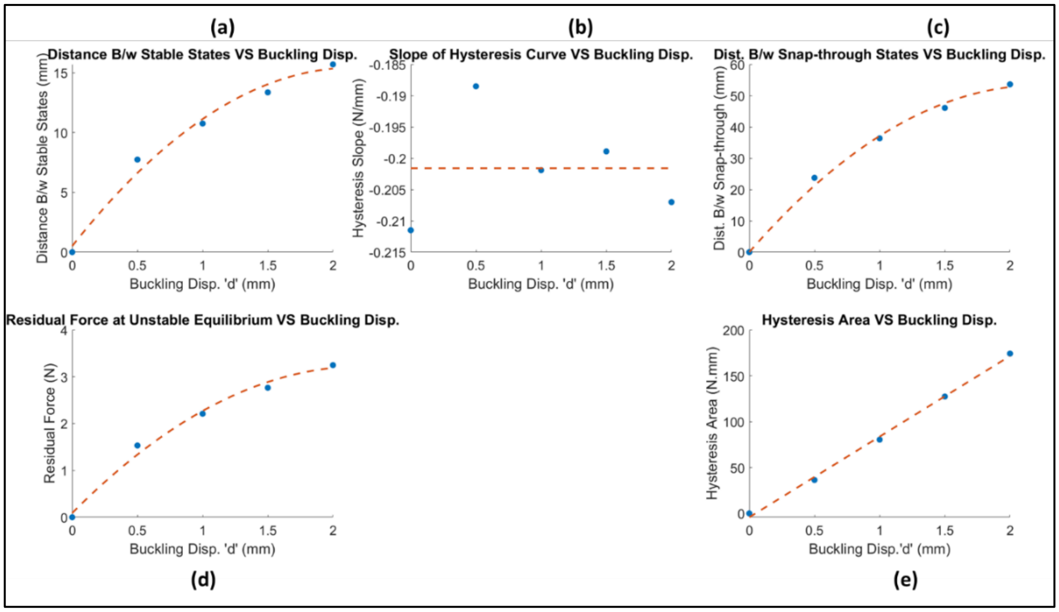

Figure 16: Variation of the parameters of the stiffness curve with the buckling displacement.

5. RESULTS AND DISCUSSIONS

Sections 2,3 and 4 presented the static behavior of the proposed BBS experimentally and numerically via finite element analysis. In this section, the experimental and FEA based stiffness curve are compared. The causes of observed discrepancies are discussed. Additionally, deductions from the sensitivity analysis are tabulated towards the end of this section.

The comparison between the stiffness curves of the experimental and the FEA analysis of the proposed BBS is shown in Figure 17. The hysteresis loop and the characteristic snap-through phenomena that was observed in the experimental BBS were successfully replicated qualitatively in the FEA analysis. However, the distance between the snap-through positions and the size of the hysteresis loop is larger in the FEA based stiffness curve. This may be due to play or compliance in the fasteners and mounting structures in the experiment that could not be accurately replicated in FEA.

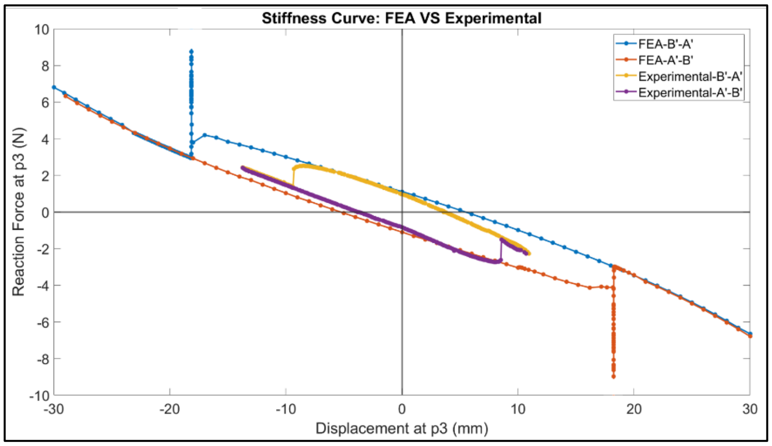

Figure 17: Stiffness curve: FEA VS experimental

Table 6 below summarizes the effects of the aspect ratio, thickness and the buckling displacement on the various features of the stiffness curve. The relationships between the above stated parameters and the features of the stiffness curve are summarized along with their respective coefficient of determination (R^2) which ranges from 0-1 and provides information on the goodness of the fit of the relation developed.

Table 6: Parameters and features

Stiffness Curve Features **Parameters**		**Dist. B/w Stable Equilibrium States. (mm)**	**Avg Slope of the Hysteresis Curve (N/mm)**	**Dist. B/w Snap Through States (mm)**	**Residual Force at Unstable Equilibrium (N)**	**Approx Hysteresis Area (N.mm)**
		y_1	y_2	y_3	y_4	y_5
Aspect Ratio	x_1	$x_1 \uparrow, y_1 \uparrow$	$x_1 \uparrow, y_2 \uparrow$	$x_1 \uparrow, y_3 \downarrow$	$x_1 \uparrow, y_4 \downarrow$	$x_1 \uparrow, y_5 \downarrow$
Relation		$y_1 = 1.97x_1 + 4.52$	$y_2 = 0.056x_1^3 - 0.69x_1^2 + 2.9x_1 - 4.24$	No Strong Correlation	$y_4 = 0.83x_1^2 - 7.23x_1 + 16.93$	$y_5 = 30.83x_1^2 - 268.77x_1 + 627.02$
R^2		0.994	0.9988	–	0.9767	0.9774
Thickness (mm)	x_2	$x_2 \uparrow, y_1 \downarrow$	$x_2 \uparrow, y_2 \downarrow$	$x_2 \uparrow, y_3 \downarrow$	$x_2 \uparrow, y_4 \uparrow$	$x_2 \uparrow, y_5 \uparrow$
Relation		$y_1 = -2.24x_2 + 11.44$	$y_2 = -3.43x_2 + 0.85$	$y_3 = -28.56x_2 + 44.89$	$y_4 = 36.16x_2 - 8.9$	$y_5 = 1045.7x_2 - 238.95$
R^2		0.9979	0.9818	0.9959	0.9847	0.9914
Buckling Displacement (mm)	x_3	$x_3 \uparrow, y_1 \uparrow$	No effect	$x_3 \uparrow, y_3 \uparrow$	$x_3 \uparrow, y_4 \uparrow$	$x_3 \uparrow, y_5 \uparrow$
Relation		$y_1 = -3.2x_3^2 + 13.82x_3 + 0.51$	$y_2 = -0.2016$	$y_3 = -10.74x_3^2 + 47.86x_3$	$y_4 = -0.63x_3^2 + 2.81x_3 + 0.09$	$y_5 = 87.9x_3 - 4.21$
R^2 / Std. Dev		0.9849	$Std.Dev = 0.0078$	0.9949	0.9894	0.9976

The relationship between the 'buckling displacement (x_3)' and the 'distance between snap-through states (y_3)' suggests that achieving a y_3 value of 17.82 mm (the distance between snap-through states in the experimental stiffness curve) is feasible in FEA when the buckling displacement is 0.41 mm.

Figure 18 and Table 7 present a comparison between the experimental stiffness curve, based on the dimensions and assembly parameters illustrated in Figure 1, and a stiffness curve generated through FEA. The FEA model replicates all the experiment's dimensions and assembly parameters but uses a buckling displacement value of 0.41 mm instead of 1 mm. Table 7 shows a maximum error of only about ~20% as opposed to the large error in observed in Figure 17 strengthening the determination that assuming all other parameters are the same in the experimental and FEA based set-up, the experimental BBS is likely undergoing a reduction in the effective buckling displacement due to wear, which is resulting in a smaller hysteresis loop.

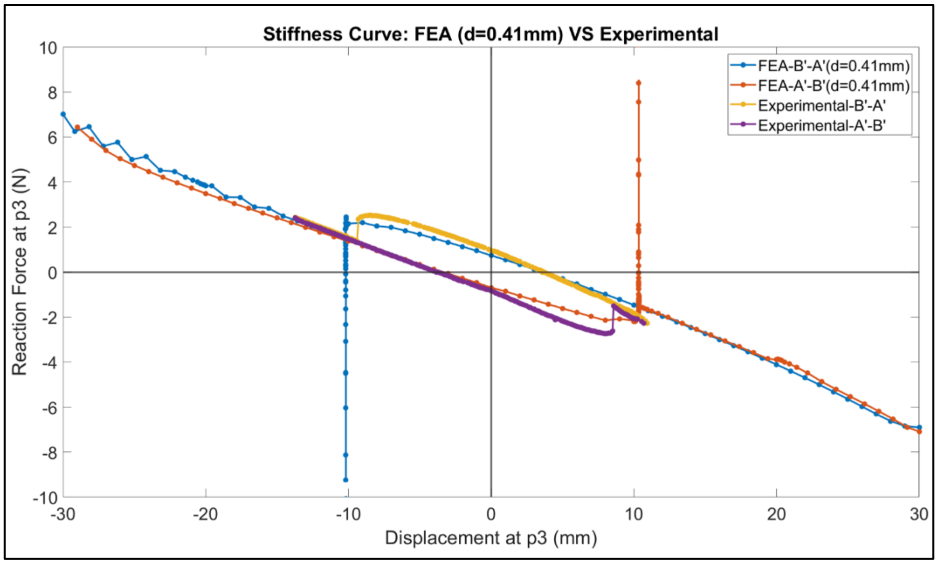

Figure 18: Experimental stiffness curve for buckling displacement of 1mm compared to FEA based stiffness curve using a buckling displacement of 0.41mm.

Table 7: Comparison between experimental stiffness curve for a buckling displacement of 1mm and FEA based stiffness curve for a buckling displacement of 0.41mm

Features of the Stiffness Curve	**Experimental Stiffness Curve (d=1mm)**	**FEA Based Stiffness Curve (d=0.41mm)**	**Percentage Difference (%)** $\left(\frac{(Exp-FEA)\times 100}{Exp}\right)$
Distance Between Stable Equilibrium States. (mm)	7.43	6.96	6.33
Avg Slope of the Trendlines of the Hysteresis Curve (N/mm)	-0.21	-0.191	8.17
Distance Between Snap Through States (mm)	17.82	20.53	-15.21
Residual Force at Unstable Equilibrium (N)	1.80	1.43	20.56
Approximate Hysteresis Area (N.mm)	32.08	29.36	8.48

6. CONCLUSION

In this paper, the static behavior of a bio-inspired bistable structure for energy harvesting has been investigated. The snap-through phenomenon and the hysteresis loop were identified as the unique characteristics of these structures. Small displacement increments (0.1-0.2mm) were applied during the experimental stiffness curve measurements to maintain the system in quasistatic equilibrium, which ensured repeatable and reliable results. The stiffness curve exhibited a complex geometry that allowed for the identification of five main features, namely (1) the distance between stable equilibrium states, (2) the average slope of the trendlines of the hysteresis curve, (3) the distance between snap-through states, (4) the residual force at unstable equilibrium, and (5) the approximate size of the hysteresis curve area.

The FEA model based on the experiment's dimensions and assembly parameters qualitatively replicated the snap-through and hysteresis loop. However, two out of the five stiffness features exhibited large errors. These discrepancies in the experimental stiffness curve and the FEA based stiffness curve can be attributed to the variations in the buckling displacement, unaccounted compliance in experimental set-up, and potential variations in material properties. A different FEA model based on the experiment's dimensions and assembly parameters except for the buckling displacement, which was set at 0.41 mm showed a maximum error of only about ~20%, which is significantly lower large error observed when the distance was set to 1 mm. This observation confirms the notion that assuming all other parameters are the same in the experimental and FEA based set-up, the experimental structure is likely undergoing a reduction in the effective buckling displacement due to wear, which is resulting in a smaller hysteresis loop.

The sensitivities of the stiffness curve to the assembly parameter of buckling displacement and geometrical parameters of thickness and aspect ratio were also investigated. A notable observation is the sensitivity of the snap through feature of the stiffness curve to the buckling displacement and aspect ratio; small changes in buckling displacement led to significant changes in the position where the snap-through phenomenon occurs, while the aspect ratio is observed to have a minimal impact on the snap-through position. The distance between the snap-through states varied quadratically with the buckling displacement. Another notable observation is that the slope of the stiffness curve is not related to the buckling displacement. Finally, it was demonstrated that each of the geometrical and assembly parameters of the proposed structure influences multiple features of the stiffness curve. Hence, it may be necessary to develop a simplified analytical modeling of the BBS to predict its stiffness response to enable its optimal design.

ACKNOWLEDGEMENTS

The authors would like to express their sincerest gratitude to the National Science Foundation for their generous support through the NSF Grant 1935951. This funding has been instrumental in advancing our understanding of the bistable energy harvesting systems. We also extend our appreciation to Dr. Daniel Deng for his guidance in this project. Dr. Deng's contributions have been invaluable for the completion of this work.

REFERENCES

[1] World Bank, 2017. The potential of the Blue Economy: Increasing long-term benefits of the sustainable use of marine resources for small island developing states and coastal least developed countries. World Bank, Washington DC.

[2] De La Torre, P. R., K. N. Salama, M. L. Berumen, E. L. Smith, and OCEANS 2012 MTS/IEEE - YEOSU Yeosu, South Korea 2012 May 21 - 2012 May 24. 2012. "The Integrated Satellite-Acoustic Telemetry (iSAT) System for Tracking Marine Megafauna." In 2012 Oceans - Yeosu, 1–4. https://doi.org/10.1109/OCEANS-Yeosu.2012.6263512.

[3] De La Torre, Pedro R., E. Lloyd Smith, Ajay Sancheti, Khaled N. Salama, Michael L. Berumen, and 2013 MTS/IEEE OCEANS Bergen, Norway 2013 June 10 - 2013 June 14. 2013. "iSAT: The Mega-Fauna Acoustic Tracking System." In 2013 MTS/IEEE OCEANS - Bergen, 1–6. https://doi.org/10.1109/OCEANS-Bergen.2013.6608085.

[4] Almansouri, Abdullah Saud, Khaled Nabil Salama, and Jurgen Kosel. n.d. "Magneto-Acoustic Resonator for Aquatic Animal Tracking." IEEE Transactions on Magnetics PP (99). https://doi.org/10.1109/TMAG.2018.2861980.

[5] Deng, Zhiqun, Thomas J. Carlson, Huidong Li, Jie Xiao, Mitchell J. Myjak, Jun Lu, Jayson J. Martinez, et al. 2015. "An Injectable Acoustic Transmitter for Juvenile Salmon." Scientific Reports 5. https://doi.org/10.1038/srep08111.

[6] Lu, J, Z D Deng, H Li, M J Myjak, J J Martinez, J Xiao, R S Brown, and S S Cartmell. 2016. "A Small Long-Life Acoustic Transmitter for Studying the Behavior of Aquatic Animals." The Review of Scientific Instruments 87 (11): 114902.

[7] Alqaleiby, Hossam, Mahmoud Ayyad, Muhammad R. Hajj, Saad A. Ragab, and Lei Zuo. 2024. "Effects of Piezoelectric Energy Harvesting from a Morphing Flapping Tail on Its Performance." Applied Energy 353. https://doi.org/10.1016/j.apenergy.2023.122022.

[8] Cha, Youngsu, Woojin Chae, Hubert Kim, Horace Walcott, Sean D. Peterson, and Maurizio Porfiri. 2016. "Energy Harvesting from a Piezoelectric Biomimetic Fish Tail." Renewable Energy 86: 449–58. https://doi.org/10.1016/j.renene.2015.07.077.

[9] Li, Huidong, Chuan Tian, Jun Lu, Mitchell J Myjak, Jayson J Martinez, Richard S Brown, and Zhiqun Daniel Deng. 2016. "An Energy Harvesting Underwater Acoustic Transmitter for Aquatic Animals." Scientific Reports 6: 33804. https://doi.org/10.1038/srep33804.

[10] Feng Qian, Mingyi Liu, Jianuo Huang, Jiajun Zhang, Hyunjun Jung, Zhiqun Daniel Deng, Muhammad R. Hajj, and Lei Zuo "Bio-inspired bistable piezoelectric energy harvester for powering animal telemetry tags: concept design and preliminary experimental validation", Proc. SPIE 11588, Active and Passive Smart Structures and Integrated Systems XV, 1158819 (22 March 2021); https://doi.org/10.1117/12.2582609

[11] Yang, Yang, Robbert Elsinghorst, Jayson J. Martinez, Hongfei Hou, Jun Lu, and Zhiqun Daniel Deng. “A Real-Time Underwater Acoustic Telemetry Receiver with Edge Computing for Studying Fish Behavior and Environmental Sensing.” IEEE Internet of Things Journal 9, no. 18 (2022). https://doi.org/10.1109/JIOT.2022.3164092.

[12] Li, Huidong, Zhiqun Daniel Deng, Jun Lu, Jayson J. Martinez, Bingbin Wu, and Xiaoqin Zang. “A New Miniaturized Acoustic Transmitter for Marine Animal Tracking.” IEEE Journal of Oceanic Engineering PP, no. 99 (2023). https://doi.org/10.1109/JOE.2023.3259147.

[13] R L Harne and K W Wang (2013) A Review of the Recent Research on Vibration Energy Harvesting via Bistable Systems. Smart Mater. Struct. 22 023001.

[14] Pellegrini, Sergio P, Nima Tolou, Mark Schenk, and Just L Herder. 2013. “Bistable Vibration Energy Harvesters: A Review.” Journal of Intelligent Material Systems and Structures 24 (11): 1303–12. https://doi.org/10.1177/1045389X12444940.

[15] Qian, Feng, Muhammad R. Hajj, and Lei Zuo. “Bio-Inspired Bi-Stable Piezoelectric Harvester for Broadband Vibration Energy Harvesting.” Energy Conversion and Management 222 (n.d.). https://doi.org/10.1016/j.enconman.2020.113174.

[16] Pan, Diankun, Zhangming Wu, Fuhong Dai, and Nima Tolou. “A Novel Design and Manufacturing Method for Compliant Bistable Structure with Dissipated Energy Feature” 196 (2020). https://doi.org/10.1016/j.matdes.2020.109081.

[17] F Cottone, L Gammaitoni, H Vocca, M Ferrari, and V Ferrari. 2012. “Piezoelectric Buckled Beams for Random Vibration Energy Harvesting.” Smart Materials and Structures 21 (3). https://doi.org/10.1088/0964-1726/21/3/035021.

[18] Abbasi, Arefeh, Tomohiko G. Sano, Dong Yan, and Pedro M. Reis. 2023. “Snap Buckling of Bistable Beams under Combined Mechanical and Magnetic Loading.” Philosophical Transactions of the Royal Society A 381 (2244). https://doi.org/10.1098/rsta.2022.0029.

[19] Nan, Wu, He Yuncheng, and Fu Jiyang. 2021. “Bistable Energy Harvester Using Easy Snap-through Performance to Increase Output Power.” Energy 226. https://doi.org/10.1016/j.energy.2021.120414.

[20] Amor, A., A. Fernandes, and J. Pouget. n.d. “Snap-through of Elastic Bistable Beam under Contactless Magnetic Actuation.” International Journal of Non-Linear Mechanics 119. https://doi.org/10.1016/j.ijnonlinmec.2019.103358.

[21] And , B., S. Baglio, A.R. Bulsara, and V. Marletta. n.d. “A Bistable Buckled Beam Based Approach for Vibrational Energy Harvesting.” Sensors & Actuators: A. Physical 211: 153–61. https://doi.org/10.1016/j.sna.2013.12.027.

[22] Timoshenko, Stephen, and James M. Gere. Theory of Elastic Stability. Second edition, international student edition. New York, Tokyo: McGraw-Hill Book Company, Inc., ; Kogakusha Company, Ltd., 1961.

[23] Yoo, Chai Hong, and Sung Chil Lee. Stability of Structures: Principles and Applications. Amsterdam: Butterworth-Heinemann, 2011.

[24] MatWeb: Material Property Data, (www.matweb.com) (Retrieved on 5th December 2022).